Imaging issues for interferometry with CGH null correctors

James H. Burge[†], Chunyu Zhao, and Ping Zhou

College of Optical Sciences
University of Arizona
Tucson, AZ USA 85721

ABSTRACT

Aspheric surfaces, such as telescope mirrors, are commonly measured using interferometry with computer generated hologram (CGH) null correctors. The interferometers can be made with high precision and low noise, and CGHs can control wavefront errors to accuracy approaching 1 nm for difficult aspheric surfaces. However, such optical systems are typically poorly suited for high performance imaging. The aspheric surface must be viewed through a CGH that was intentionally designed to introduce many hundreds of waves of aberration. The imaging aberrations create difficulties for the measurements by coupling both geometric and diffraction effects into the measurement. These issues are explored here, and we show how the use of larger holograms can mitigate these effects.

Keywords: Interferometry, computer generated holograms, aspherics

1. INTRODUCTION

Aspheric optical surfaces can be measured to high accuracy using interferometry with computer generated hologram (CGH) null correctors. The CGH is optimized for wavefront performance, and not for good imaging. The surface itself is always viewed through the CGH null corrector, which causes significant distortion and aberrations. The distortion is has been discussed elsewhere,[1,2] and can be fully corrected by morphing or un-distorting the data.[3]

The imaging aberrations due to the CGH are dominated by second order effects, which are described using field curvatures. In general, the images suffer defocus and astigmatism which vary across the focal plane. This aberration couples with diffraction to cause two principal problems with the measurement:

- High frequency data is filtered out. We treat this phase smoothing using a small-phase approximation to the well-known Talbot imaging relations.

- Diffraction ripples from the edges introduce measurement artifacts. We treat this effect using Fresnel integrals.

The field curves created by the imaging through the CGH are equivalent with a focus error projected into the two principal directions (S and T for an axisymmetric system). The two diffraction effects then have dependency on the orientation of the ripples or the edge with respect to the S and T directions. These effects are analyzed using equivalent propagation distance and coordinate transformations.

This paper builds on previous work from the authors. A model for diffraction effects for refractive null correctors was developed by Zhao and Burge[4]. This has been further expanded by applying the generalized Coddington relations[5] to include the special issues with diffractive null correctors.[6] Section 2 presents a summary of the geometry and imaging aberration specific to CGH null testing of conic mirrors. The detailed derivations and analysis for this section are published by the authors elsewhere.[7] We provide background for the diffraction effects for coherent systems such as interferometers in section 3. Section 4 presents the general method of coupling the diffraction effects with the imaging aberrations that arise from the use of CGHs. The specific example of null testing a 1.35 meter off axis segment of a 6.5-m diameter paraboloidal mirror is provided in Section 5.

[†]J. H. Burge is Professor of Optical Sciences and Astronomy, University of Arizona. 520-621-8182, jburge@optics.arizona.edu

2. IMAGING ABERRATIONS FROM CGH NULL CORRECTORS

The null corrector used for measuring aspheric surfaces compensates for the aspheric departure of the surface. I single computer generated hologram (CGH) is commonly used as a null corrector because of its low cost and high accuracy. Practically, the CGH converts a spherical wavefront from the interferometer to an aspheric wavefront that propagates such that the shape of the wavefront matches the aspheric shape of the mirror. Then this wavefront will reflect back on itself and give a null test. One of the special properties of spheres that makes them easy to measure is that a spherical wavefront stays spherical as it propagates. Only the radius of curvature changes as the light propagates.

The measurement of the aspheric surface also requires the interferometer to view the surface through the null corrector. In order to make sharp images of any features on the mirror being measured, the image quality must be good. Since a particular CGH is designed based on the wavefront shape, there are no additional degrees of freedom left to improve the image quality. In fact, if the position of the CGH along the cone of light defined by the aspheric surface is fixed, there is very little freedom to choose the CGH phase function. The position of the point source with respect to the CGH provides the only degree of freedom, but there exists only a small range of possibilities that will allow separation of the different orders of diffraction and minimize sensitivity to CGH errors. Once the CGH phase function is defined, the imaging properties for the interferometer viewing through the CGH can be calculated.
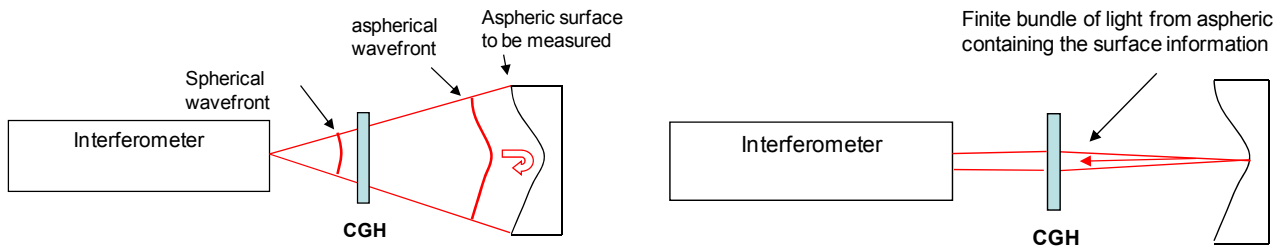

Figure 1. The CGH null corrector converts the spherical wavefront from the interferometer to an aspheric wavefront that propagates to fit the surface under test. To create an image of the part, the interferometer must view through the CGH. The spatial frequency content of the wavefront reflected from the surface determines the size of the equivalent bundle of light that must be imaged.

2.1 Parametric model for CGH null correctors

The design of the CGH null corrector is fully defined by the geometry, i.e. the relative position of the interferometer, CGH, and the mirror under test. As such, we can develop parametric relations that define the CGH as functions of these parameters. We present these relations here, but the derivation is published elsewhere by the authors.[7] Figure 2 shows the geometry of CGH null test for a conic surface, assuming axisymmetry. The hologram is placed distance h away from the paraxial center of curvature, and the interferometer focus is located at point E, a distance p from the CGH. The phase function for the CGH is calculated to maintain a constant optical path difference from the mirror, projected in a direction normal to its surface, to point E. The conic surface is fully defined with two parameters, the vertex radius of curvature R and the conic constant K. A paraboloidal surface will have $K = -1$.
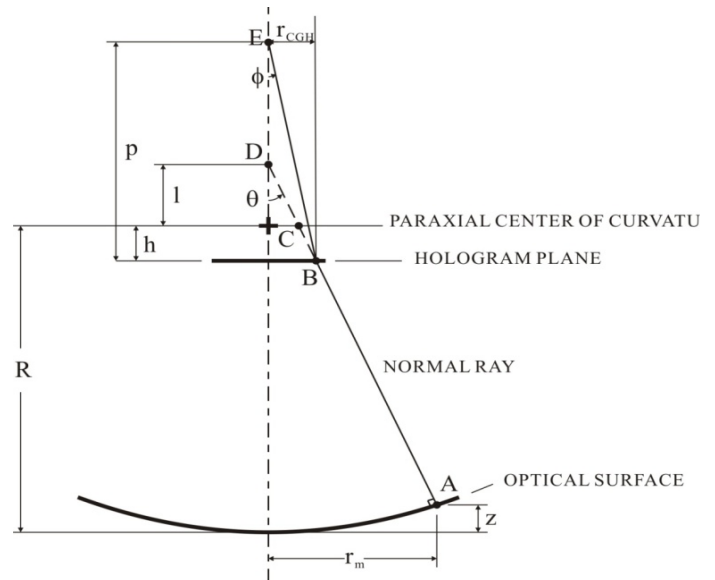

Figure 2. Geometry definition for CGH test of aspheric mirror.

The conic optical surface is given by

$$z(r) = \frac{r_m^2}{R + \sqrt{R^2 - (K+1)r_m^2}} \ , \tag{1}$$

where r_m is the radial position on the test surface. The phase function of the CGH is described by geometry, and approximated to the fourth order as

$$\Phi(r_m) = (R-h) + p - AB - \frac{p}{\cos(\phi)}$$
$$= \frac{\left(-h^2 + hp\right)r_m^2}{2pR^2} + \frac{\left(h^4 - 4h^2 p^2 - 4h^2 Kp^2 + 3hp^3 + 4hKp^3 + 4hKp^2 R - 3Kp^3 R\right)r_m^4}{8p^3 R^4} \ . \tag{2}$$

Also, the CGH diameter is approximated as

$$D_{cgh} = \frac{2hr_{max}}{R} + \frac{(h + hK - KR)r_{max}^3}{R^3} \ , \tag{3}$$

where r_{max} is the maximum value of r_m, or equivalently, it is one half of the mirror diameter.

2.2 Imaging distortion

The first order effect of imaging through CGHs is mapping distortion, which means the mapping from the test optic to the interferogram is not linear. The imaging distortion from a null corrector will cause three complications: one is that the surface defects appear shifted; the second is that lower order alignment errors appear as higher order wavefront errors; the third problem is that diffraction effects, which depend on spatial frequency, will vary as the magnification changes with position and orientation.

Mapping distortion can be quantified as nonlinear magnification in the radial and circumferential directions. Since this distortion requires mapping to image space, we assume the interferometer has ideal imaging with effective focal length f. By taking derivatives of the functions above, we develop relationships for the magnification in the two principal directions : m_r in the radial, and m_a in the azimuthal directions,

$$m_r = \frac{dr_{image}}{dr_m} = \frac{f}{p}\left(\frac{h}{R} + \frac{3(h + hK - KR)}{2R^3}r_m^2\right)$$
$$m_a = \frac{r_{image}}{r_m} = \frac{f}{p}\left(\frac{h}{R} + \frac{(h + hK - KR)}{2R^3}r_m^2\right) \ . \tag{4}$$

2.3 Imaging aberrations

Performing a Taylor expansion on the imaging relations with respect to pupil, the next term after the linear term defining mapping is quadratic. Such aberrations take the form of focus and astigmatism, and their field dependence is quantified by field curves which designate the location where a small bundle of light will come to focus for each of the principal directions. We determine the field curvatures from the two second derivatives for the axisymmetric hologram phase function Φ. One is in the radial direction C_r and the other C_a is in the azimuthal direction, perpendicular to the radial direction. The two curvatures in the hologram coordinates are

$$C_r(r_m) = \frac{d^2\Phi}{dr_{CGH}^2} = \frac{d^2\Phi}{dr_m^2} \cdot \left(\frac{dr_m}{dr_{CGH}}\right)^2 - \frac{d\Phi}{dr_m}\frac{d^2 r_{CGH}}{dr_m^2}\left(\frac{dr_m}{dr_{CGH}}\right)^3$$
$$C_a(r_m) = \frac{1}{r_{CGH}}\frac{d\Phi}{dr_{CGH}} = \frac{1}{r_{CGH}}\frac{d\Phi}{dr_m} \cdot \frac{dr_m}{dr_{CGH}} \ . \tag{5}$$

The two principal curvatures C_r and C_a bring the light to the tangential and sagittal focal planes respectively for the axisymmetric system. This can be confusing because the "tangential focus" by this definition comes from curvature in the radial direction and the "sagittal focus" comes from the curvature in the circumferential direction. We maintain the "T" and "S" definition for the field curves, but refer to C_t as the radial curvature and C_a as the azimuthal or circumferential curvature. When a small bundle of rays originating from a point on the test surface are incident on the hologram, the rays see different phase curvatures. The fans in the radial and circumferential directions will focus onto separate curved surfaces because of the field curvature and astigmatism imaging aberrations from the CGH. These field curvatures can be obtained in commercial raytracing software or calculated by using generalized Coddington equations[5], which are

$$\frac{\cos^2 \phi}{t'} - \frac{\cos^2 \theta}{t} = C_r,$$
$$\frac{1}{s'} - \frac{1}{s} = C_a$$

(6)

where t and s are the physical distance from the test surface to the hologram, and t' and s' are the distance from the hologram to the tangential image point and sagittal image point, and θ and ϕ are the incident and exitant angles shown in Figure 2.

To evaluate the coupling of diffraction with the field curvature, we create an image at an equivalent collimated space by inserting an ideal lens with a focal lens of f at one focal length away from the point focus. This construction is useful because it simplifies the analysis, but it is not necessary and the value chosen for the focal length itself is arbitrary, which will be normalized out of the result. An ideal lens preserves the field curves and creates a collimated wavefront, and telecentric image.

When the distance between the hologram and the paraxial focus h and the distance between the hologram and the point focus p are small compared to the radius curvature of the test piece R, the field curves are mostly quadratic in field. We can use the geometric imaging relationship to calculate the field curves. Keeping the dominant terms, the quadratic approximation for the two field curves are determined to be

$$t_i' \approx \frac{3f^2 K}{2p^2 R} r_m^2$$
$$s_i' \approx \frac{f^2 K}{2p^2 R} r_m^2$$

(7)

3. GEOMETRICAL EFFECTS OF IMAGING ABERRATIONS

The geometrical effects of image aberrations are well known and discussed briefly here. The two principal effects are from mapping distortion and retrace errors.

3.1 Geometric effects of distortion

Distortion in the image for a null test of an aspheric surface creates a nuisance, but does not by itself cause a measurement limitation. The magnitude of the distortion is predicted by the relations above, and can be seen graphically below. The distortion is a strong function of the CGH position, which defines the CGH size. In general, larger CGHs have less imaging distortion. This is apparent in Figure 3.

The effects of distortion are mitigated by remapping or "morphing" the data. This is done by placing reference marks on the optic under test and locating their position in the image.[8] Mapping relations are derived by fitting polynomial functions to the data to provide a transformation of the distorted data back to real coordinates. We have developed an orthonormal vector basis[3], defined by derivatives of Zernike polynomials, for this purpose.
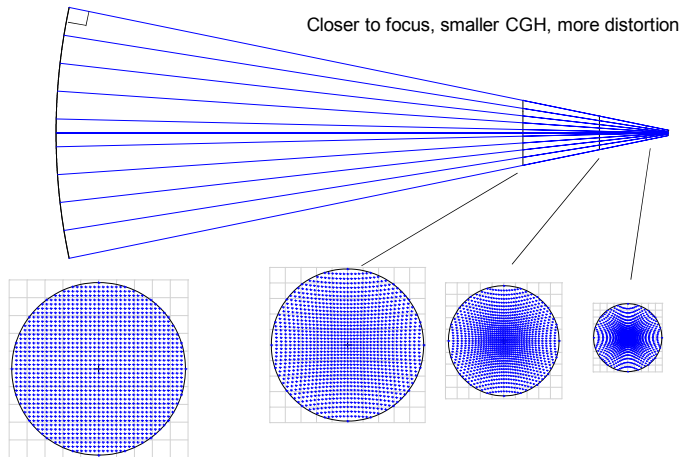
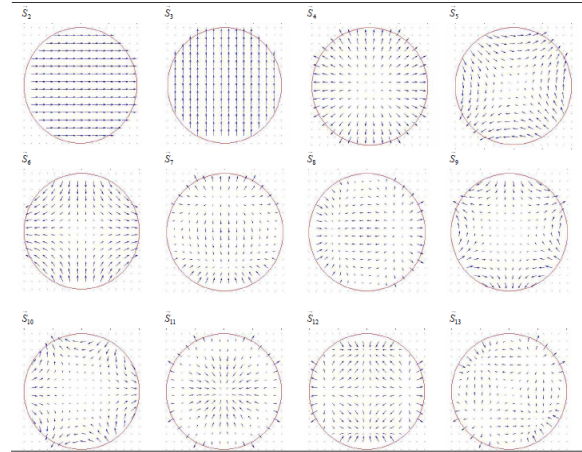Figure 3. Distortion can be seen directly from the ray trace.

Figure 4. Zhao-Burge orthonormal vector basis[3] for describing mapping distortion.

3.2 Geometric effects of aberrations coupled with surface slopes

A second geometric effect of imaging aberrations couples the slope variations of the surface under test with the aberrations to create errors. This basic effect has been treated elsewhere.[2] These effects become very important where the measurements are made with large amounts of low order mirror shape departure from nominal. The errors are proportional to the slope departure of the mirror from the ideal. Since the null lens is specifically designed to create an ideal wavefront that matches the mirror, this effect is not significant for most null testing. This effect is very important for "non-null" testing where mild aspheres are measured using a spherical wavefront.

4. DIFFRACTION EFFECTS OF IMAGE ABERRATIONS

4.1 Interferometer imaging system

The imaging performance through the CGH is difficult to evaluate because it is part of a coherent system. For standard incoherent imaging, light is assumed to come from each point in the object and propagate in all directions. Some of the light makes it into the optical system, and is used for imaging. The aperture stop in the system defines which rays from the object will be used to create the image.[4] The imaging for most interferometers is fundamentally different. The light starts at a point source, and follows only refraction and reflection to the surface under test, then to the final image. The aperture stop in the system does not nominally define the light that makes it to the image. For this fully coherent system, it is convenient to think of one ray per point on the mirror. The ray will propagate to the image plane and define the image. Only for the case of large slope errors or high frequency ripple does the stop have any effect.

This fully coherent model leaves no room for imaging aberrations to degrade the image. Each ray will intersect the image plane at a sharp geometric point. We treat the imaging system using an infinitesimal bundle of rays, because when a ray reflects from a surface with some structure, a bundle of rays is created due to scattering and diffraction. These rays originate from each point on the surface under test. The width of the bundle can be defined in the computer model using the size of the stop at the focus in the interferometer. The stop, acting as a low-pass filter, limits the amount of the light that can make it to the detector. For incoherent imaging system, diffraction effects are washed out. For coherent imaging systems, diffraction effects influence interferometric measurements by smoothing actual phase irregularities and introducing phase errors due to edge diffraction.

4.2 Phase smoothing analysis using Talbot model

Diffraction effects cause a change in high spatial frequency components, which we call phase smoothing, which is describe using the Talbot imaging theory[9]. Talbot imaging is a diffraction phenomenon that occurs for a monochromatic wavefront with a periodic complex amplitude. If a wavefront with complex amplitude of a period of d is illuminated by collimated light, then that same complex amplitude is formed by free space diffraction at integer multiples of the Talbot distance $z_T = 2d^2/\lambda$. As a sinusoidal phase pattern propagates, it will cycle through a reverse contrast amplitude pattern, a conjugate phase pattern, a pure amplitude pattern, then back to the original phase pattern.

If a wavefront with small phase ripples of W ($W \ll 1$) waves propagates a distance of L in collimated space, then the magnitude of the ripples will be attenuated to W'. A transfer function can be defined as

$$TF = \frac{W'}{W} = \cos\left(2\pi \frac{L}{z_T}\right) = \cos\left(\frac{\pi\lambda L}{d^2}\right), \tag{8}$$

which can be used to predict the attenuation in high frequency (small scale) ripples due to propagation.

The Talbot distance z_T is defined for a collimated beam. For a spherical beam, it is convenient to convert it into an equivalent collimated beam and then use the Talbot effect to predict how wavefronts change due to propagation. The diffraction pattern for a spherical beam is the same as that observed for a collimated beam, except that the diffraction pattern occurs at the *effective propagation distance L_e*, and it is scaled in the transverse dimension.

The effects of imaging aberrations are analyzed by coupling quadratic aberrations, quantified by the field curves, with the phase smoothing and edge diffraction presented above. The field curves show defocus, or equivalent propagation in the image space as functions of field position and orientation. The diffraction effects can be treated at each field point and orientation as propagation of light from its focused position given by the field curve to the focal plane. This is apparent for the principal S and T orientation. The case with general orientation is provided elsewhere[7].

We simplify the problem using the concept of ideal lenses to transfer from one plane to another. If the wavefront ripples are imaged faithfully from one space to another, there is no attenuation from the Talbot effect and no edge effects. The magnitude of the amplitude and phase distributions will be preserved. For the plane that is out of focus, the Talbot effect described above can be used to determine the change in phase due to the propagation. In any re-imaged optical space, the propagation distance equals the out of focus distance. The spatial period of the ripples must correctly include the magnification of the image. The same principle applies for the field curves, but this includes variation across the image of the test surface and it includes a defocus in the circumferential and radial directions. The defocus across the field is given by the field curves, and the two curves correspond to the image with ripples that are radial or circumferential. Interferometers can only focus one plane at a time so that the other field will be out of focus.

We evaluate the phase smoothing effect at an arbitrary image plane, normalizing the spatial frequency $f_{normalized}$ to cycles/diameter. We combine the defocus effect of the field curves with the magnification variation and Talbot smoothing to create a transfer function at a telecentric image,

$$TF(r_m) = \cos\left[\frac{\pi\lambda f_{normalized}^2}{4a^2 m(r_m)^2} \Delta z(r_m)\right], \tag{9}$$

where ,

$\Delta z(r_m)$ is the defocus, which is provided for the principal directions as the field curves,
$2a$ is the mirror diameter, and
$m(r_m)$.is the local magnification for the image as a function of the mirror position.

The development of the transfer function for sinusoidal ripples in an arbitrary direction is provided elsewhere.[7]

We combine the above relations to provide parametric relations for phase smoothing effect. We define the test surface using two radii, r_{min} and r_{max}. If we focus on the inner edge of the test surface, the transfer function for the phase ripples in radial and azimuthal directions are

$$TF_r = \cos\left\{\frac{3K\pi\lambda f_{\text{normalized}}^2 R^5 (r^2 - r_{\min}^2)}{2r_{\max}^2 \left[3h(1+K)r^2 - 3Kr^2R + 2hR^2\right]^2}\right\}$$

$$TF_a = \cos\left\{\frac{K\pi\lambda f_{\text{normalized}}^2 R^5 \left(r^2 - 3r_{\min}^2\right)}{2r_{\max}^2 \left[h(1+K)r^2 - Kr^2R + 2hR^2\right]^2}\right\} \qquad (10)$$

We can also define this interms of the CGH size D,

$$TF_r = \cos\left\{\frac{3K\pi\lambda f_{\text{normalized}}^2 \left[2R^2 + (1+K)r_{\max}^2\right]^2 (r^2 - r_{\min}^2)}{2R\left[3D_{cgh}(1+K)r^2 + 2D_{cgh}R^2 + 2Kr_{\max}\left(-3r^2 + r_{\max}^2\right)\right]^2}\right\}$$

$$TF_a = \cos\left\{\frac{K\pi\lambda f_{\text{normalized}}^2 \left[2R^2 + (1+K)r_{\max}^2\right]^2 \left(r^2 - 3r_{\min}^2\right)}{2R\left[D_{cgh}(1+K)r^2 + 2D_{cgh}R^2 + 2Kr_{\max}\left(-r^2 + r_{\max}^2\right)\right]^2}\right\} \qquad (11)$$

4.3 Edge effects using Fresnel integral

Edge diffraction from the test surface occurs when its edge is not in focus. The diffraction at the edge of the aperture can be modeled as the Fresnel knife-edge diffraction. The real and imaginary parts of the electric field distribution can be found by evaluating the Fresnel integrals.[10] Figure 5 shows the amplitude and phase fluctuations due to the edge diffraction. Both amplitude and phase have a rapid oscillation as the distance from the edge becomes large. The diffraction effects scale with $\sqrt{\lambda L/2}$, where L is the defocus error in a collimated wavefront space or the equivalent propagation distance in a non-collimated wavefront space.

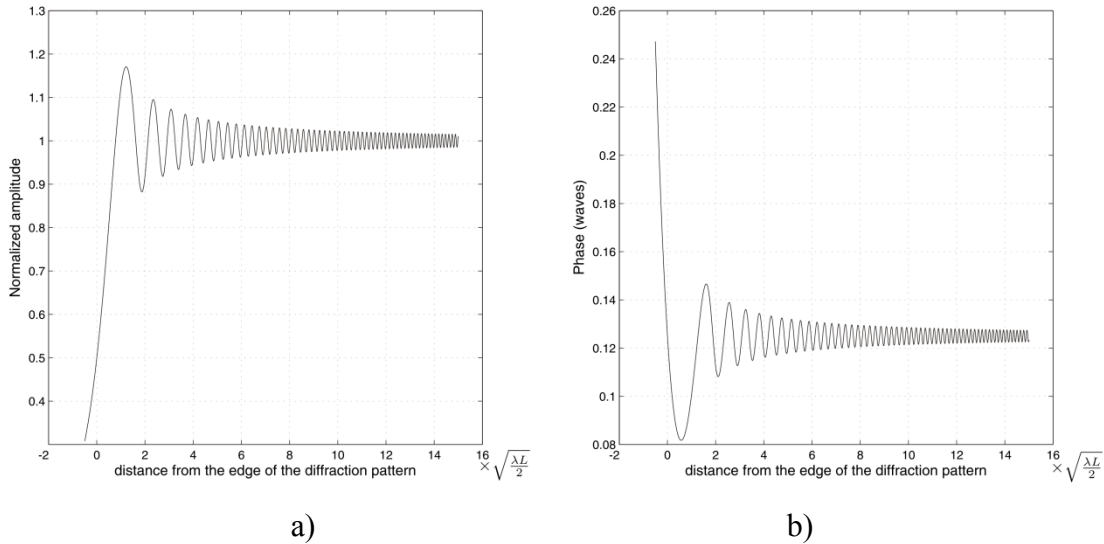a)   b)

Figure 5. The amplitude and phase variation calculated from the Fresnel integrals for the case of diffraction of collimated

light from a knife edge.

The severity of effect of edge diffraction can be described by the *diffracted edge ratio*:

$$\varepsilon = \frac{5\sqrt{\lambda L/2}}{r_{image}} \quad , \tag{12}$$

which gives a normalized width of the edge diffraction For example, if the intermediate image is 50 mm in radius and it is 790 mm out of focus, then the diffracted edge ratio is 0.05 for the wavelength of 633 nm. Almost all of the edge effect occurs in the outer 5% of the radius.

We evaluate the case where the system focus is set so the radial focus is optimized at the inside edge of an annular mirror, r_{min}. For this case, the outer edge at r_{max} will be out of focus, which is quantified with the radial defocus term. The diffracted edge ratio is then

$$\varepsilon = \frac{5}{D_{cgh}} \sqrt{\left| \frac{3\lambda K}{R} \left(r_{max}^2 - r_{min}^2 \right) \right|} \quad , \tag{12}$$

where D_{cgh} is the diameter of the CGH.

5. EXAMPLE

We evaluate the CGH null test of an a 1.3-m off axis mirror segment, which is the outer segment for a 6.6-m diameter paraboloid with 16 meter radius of curvature. We look specifically at two cases: a 100 mm CGH and a 200 mm CGH. The geometry of this test, as well as a graphical depiction of the imaging distortion, are shown below in Figure 6. The CGH test is assumed to maintain axisymmetry with the parent paraboloid, but none of the results here would change significantly if this were violated.

1.3-m hex

200 mm CGH

3.3m

Interferometer position has very little impact on imaging
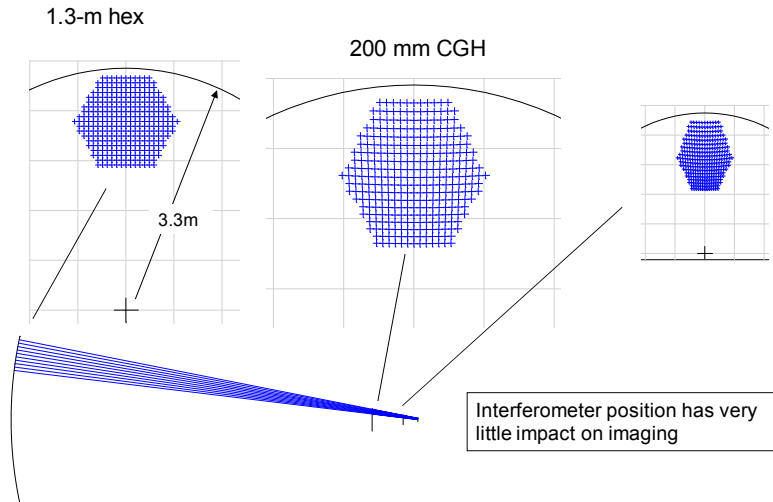
Figure 6. Layout of CGH test of an off axis hexagonal segment of a 6.6-m paraboloidal mirror with 16 meter radius of curvature.

The CGH phase functions for the parent, calculated from Eq. 2 is compared with an exact value from direct simulation in Figure 7. When plotted as functions of the mirror coordinate, the phase functions are nearly the same. The magnification variation and the second derivative variations are shown in Figure 8. Both are much more severe for the smaller CGH -- magnification variations are about 2.5x worse and variations in second derivatives are about 5 x worse. The effects are compounded when we look at the transfer functions.

The assessment of the imaging performance combines all of the issues above. To model the performance we create an image with ideal lens of focal length 200 mm and evaluate transfer functions and the edge diffraction. The actual value

of this focal length will affect intermediate calculations, but it is normalized out of the transfer function and the diffracted edge ratio.
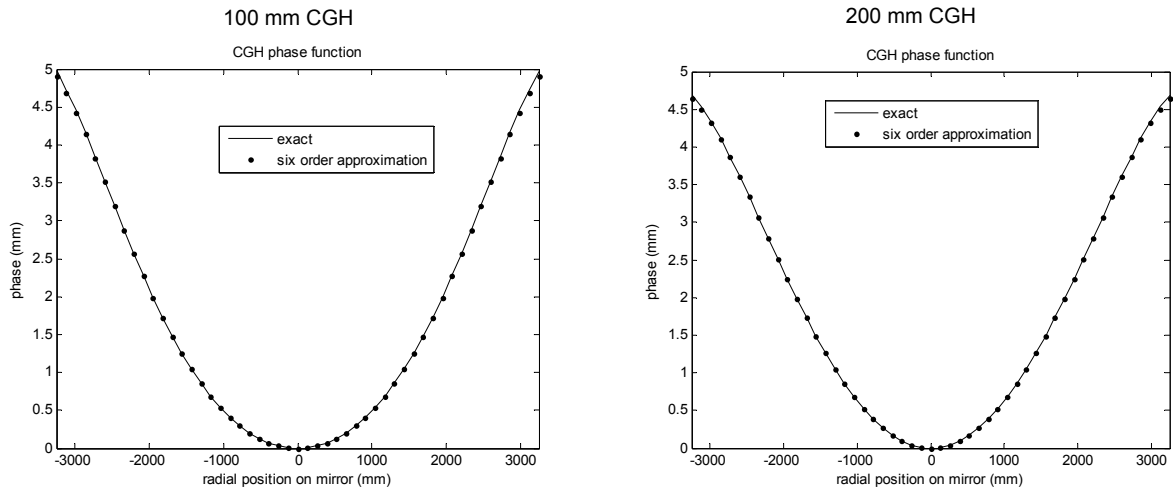

Figure 7. CGH phase function for the two cases. Here the function plotted as a function of mirror position does not change significantly from one CGH to the other.
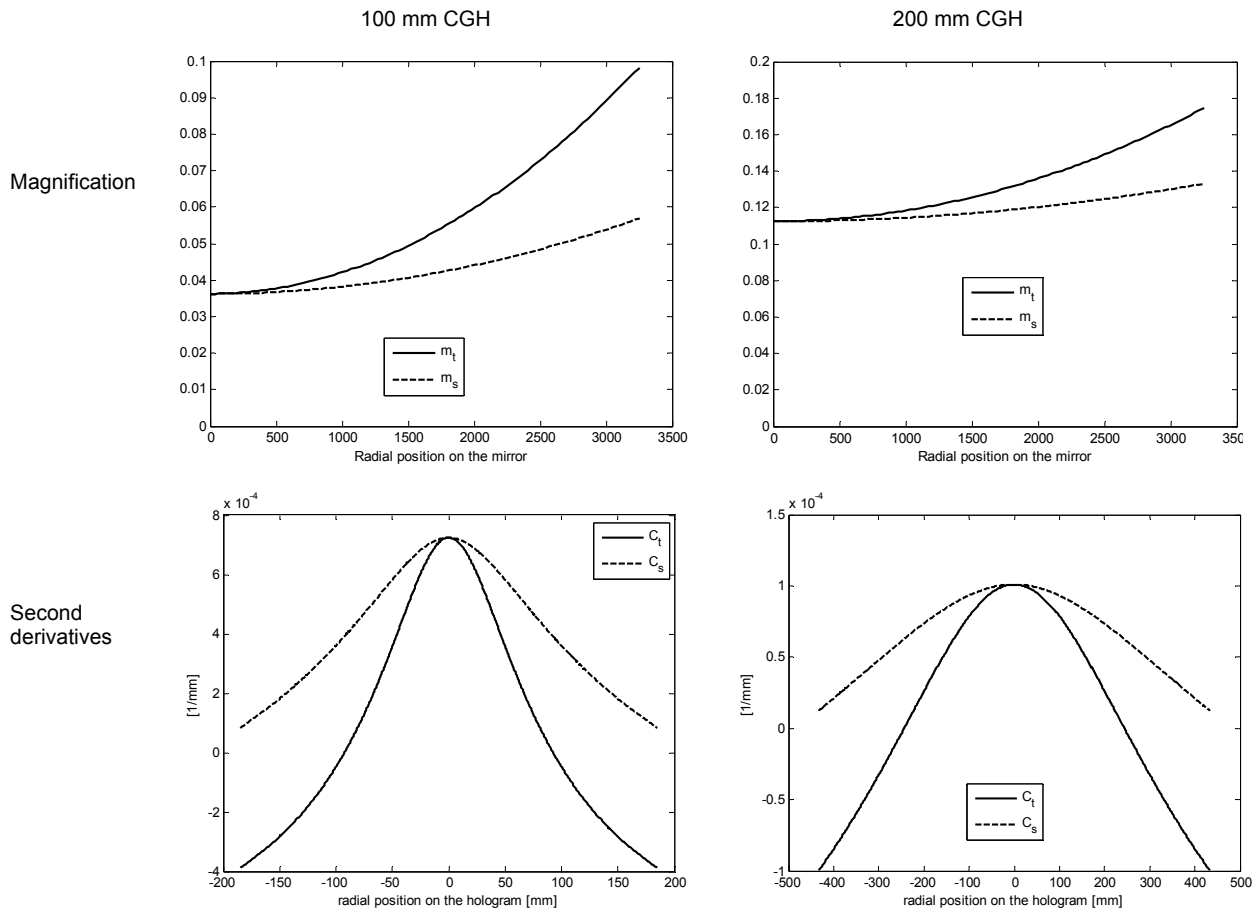

Figure 8. Magnification variation and second derivatives for the two CGHs. The "t" direction corresponds with radial and the "s" direction corresponds with azimuthal.

The analysis for the smaller, 100 mm CGH is summarized in Figure 9 for the case where the image is made with a 200 mm effective focal length lens. If radial or "T" focus is adjusted to the inner edge, 2 meters from the parent axis, then the outer edge will be out of focus by 22 mm. The transfer function for this case shows very bad performance. In fact, surface ripples with 100 cycles/m (10 mm period) will be so far out of focus that they suffer phase reversal. Bumps look like valleys. The measurement will achieve >80% TF for frequencies less 50/m at the inside edge, in the azimuthal direction and for frequencies < 75/mm at the outside edge in the radial direction. If the focus is adjusted to bring a different zone in focus, the overall performance gets considerably worse. The reason is that the nonlinear magnification causes the ripples at the edge to appear to have much higher frequency, reducing the Talbot distance. Overall performance is optimized by focusing on the inner edge.
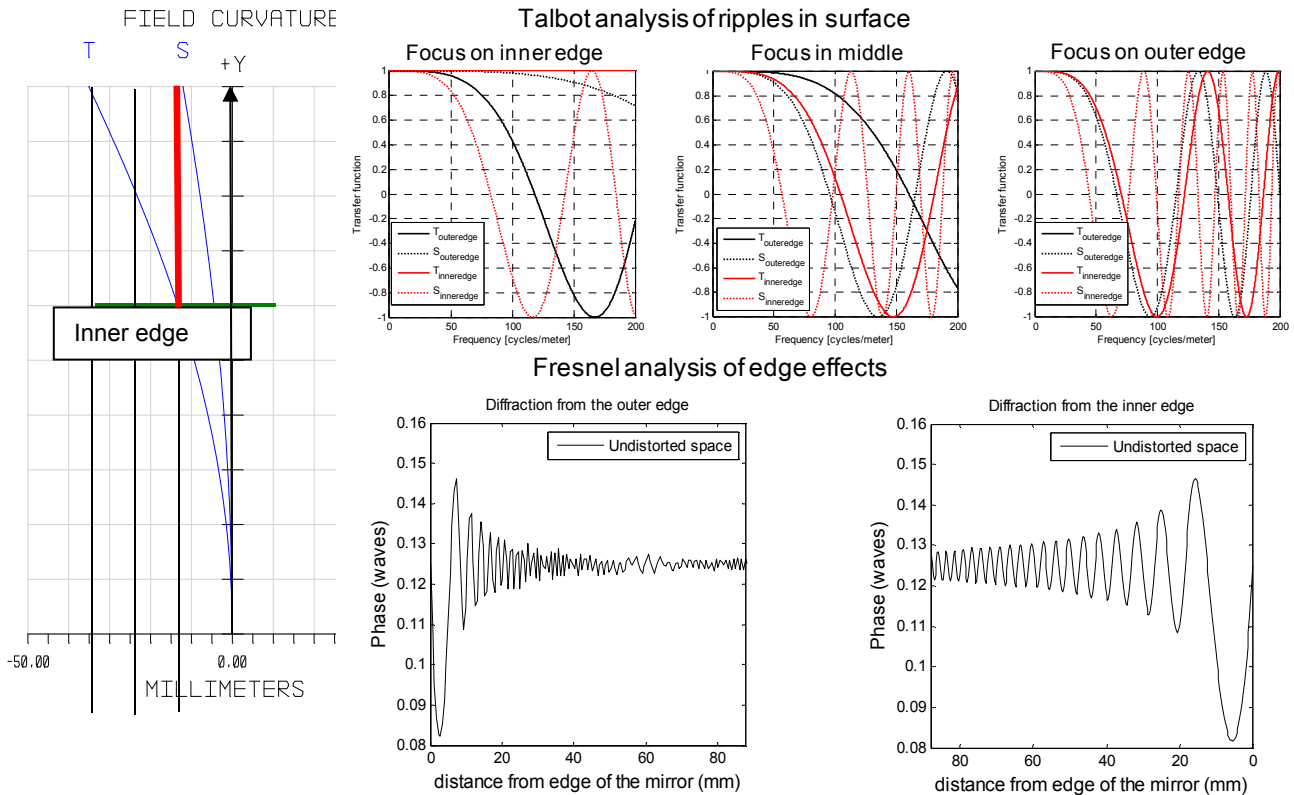

Figure 9. Imaging performance for null test using 100 mm CGH. The "T" or radial focus shows 35 mm difference between the inner and outer edge for the case with 200 mm focal length imaging lens.

The effects of edge diffraction are also seen in Figure 9. Two cases are examined, corresponding to focus on the inner edge (r = 2000 mm) and the outer edge (r = 3300 mm). As stated above, the optimal focus is set on the inner edge. At this focus position, the diffraction edge ripples at the edge of the mirror due to the 22 mm propagation extend in about 20 mm from the edge. These diffraction effects will look like real ripples in the surface with > 20 nm PV surface variation.

The analysis for the larger, 200 mm CGH, shown in Figure 10, indicates much better performance. Again the 200 mm effective focal length lens is assumed for the creation of the intermediate image. For this case, if radial or "T" focus is adjusted to the inner edge, 2 meters from the parent axis, then the outer edge will out of focus by only 4 mm, down from 35 mm for the case of the 100 mm CGH. The transfer function for this case shows much better performance. The measurement will achieve >80% TF for frequencies up to 150/m for all directions and positions on the mirror. Again, the benefit of focusing on the inside edge is clear.
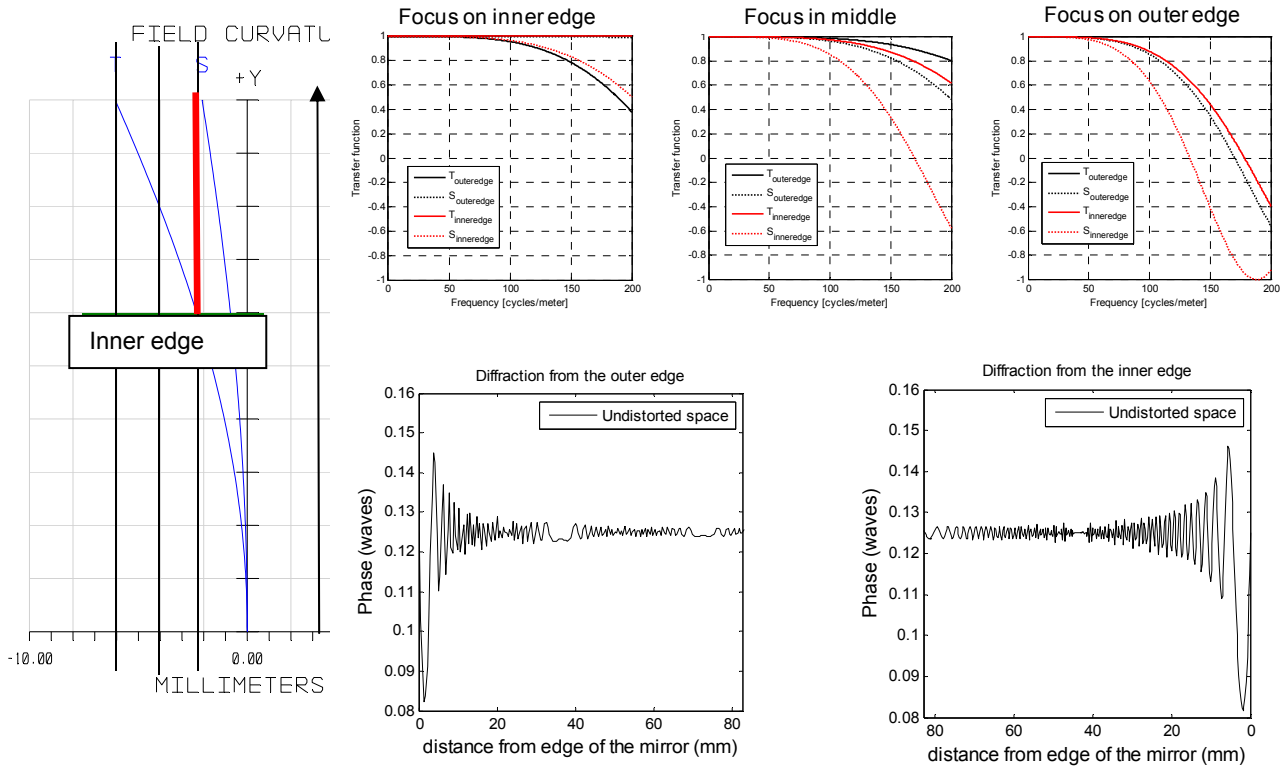

Figure 10. Imaging performance for null test using 200 mm CGH. The "T" or radial focus shows 6 mm difference between the inner and outer edge for the case with 200 mm focal length imaging lens.

The effects of edge diffraction are also seen in Figure 10. Two cases are examined, corresponding to focus on the inner edge (r = 2000 mm) and the outer edge (r = 3300 mm). As stated above, the optimal focus is set on the inner edge. At this focus position, the diffraction edge ripples at the edge of the mirror due to the 6 mm propagation extend in about 8 mm from the edge.

6. CONCLUSION

The use of computer generated holograms allows high excellent accuracy for measuring aspheric surfaces. But one should be very cautious about the diffraction effects, especially for measuring high frequency surface errors or for getting high resolution near the edge. We present a methodology for analyzing these effects in terms of a few geometric parameters and we show the great advantage that can be achieved by using larger CGHs.

REFERENCES

1) L. A. Selberg, "Interferometer accuracy and precision", Proc. SPIE **1400**, 24-32 (1990).

2) P. E. Murphy, T. G. Brown, and D. T. Moore, "Measurement and calibration of interferometric imaging aberrations," Applied Optics Vol.39, No.34, 6421-6429 (2000).

3) C. Zhao and J. H. Burge, "Orthonormal vector polynomials in a unit circle application: fitting mapping distortions in a null test," Proc. SPIE **7426**, (2009).

4) C. Zhao and J. H. Burge, "Imaging aberrations from null correctors," Proc. SPIE **6723**,67230L (2007).

5) C. Zhao and J. H. Burge, "Generalized Coddington equations for refractive/diffraction hybrid surfaces," Proc. SPIE **7652,** (2010).

6) P. Zhou, J. H. Burge, and C. Zhao, "Imaging issues for interferometric measurement of aspheric surfaces using CGH null correctors," Proc. SPIE **7790,** (2010).

7) P. Zhou, J. H. Burge and C, Zhao, "Diffraction effects for interferometric measurements due to field aberrations," to be submitted to Applied Optics (2010).

8) M. Novak, C. Zhao, and J. H. Burge, "Distortion mapping correction in aspheric null testing," Proc. SPIE **7063**, 706313 (2008).

9) P. Zhou and J. H. Burge, "Analysis of wavefront propagation using the Talbot effect," submitted to Applied Optics (2010).

10) J. Goodman, *Introduction to Fourier Optics*, Roberts and Company Publisher, 88-91 (2005).